DOI: 10.13009/EUCASS2023-929
Aerospace Europe Conference 2023 – 10TH EUCASS – 9TH CEAS

Modelling of MHD flow control for atmospheric re-entry at ONERA

Benjamin Khiar †, Fabien Tholin, François Pechereau, Landry Riou and Denis Packan
DPHY, ONERA, Université Paris Saclay, F-91123 Palaiseau
benjamin.khiar@onera.fr
†Corresponding author

Abstract

We present recent developments in modelling magnetohydrodynamics (MHD) re-entry at ONERA. By applying a magnetic field on the re-entry ionized shocked flow, electrical currents and Lorentz forces can be generated around the vehicle. These effects can be harnessed to modify the aerodynamic forces as well as to reduce the intense heat fluxes that the vehicle experiences. We provide here an overview of the different numerical tools used for simulation of MHD phenomena occurring from high altitude to low altitude regimes. Continuum regime is in particular considered, with equilibrium or non-equilibrium effects allowed. Some applications are briefly described, from modelling laboratory MHD experiments in shock tubes to reproducing MHD-assisted re-entry in martian conditions.

1. Introduction

The use of magnetohydrodynamics (MHD) to assist vehicles as they experience the challenging environment of atmospheric re-entry has been a long-standing aspiration for space mission designers. Very early after the space age started, some authors considered to take advantage of the electric properties of the shock-generated re-entry plasma to modify the flow.[1] In particular, it was quickly realized that by applying a magnetic field on the incoming plasma, the bow shock standoff distance in front of the vehicle could be repelled away from the surface.[2] As a direct consequence, the thermal heat flux could be reduced providing valuable assistance to the vehicle thermal protection system. A second aspect of the MHD interaction is the generation of a reaction force acting directly on the magnetic field generation device (magnet, coils). This force adds up to the aerodynamic forces and it was suggested this could be used as a drag enhancement mechanism, especially at high altitude where atmospheric density is too small to provide useful drag: this defines the concept of MHD aero-braking.[3] Past practical use of MHD-devices for re-entry has been hampered by limitations associated to the field-generation technologies. Nowadays, high-temperature compact superconducting technologies enables a new surge of interest in this promising solution.[4]

We present in this paper an overview of recent MHD-related numerical activities at ONERA. We first present the general model that we employ and the suite of numerical tools that is used to model MHD re-entry physics. We then separately treat some important aspects of the different regimes that are encountered during re-entry in the presence of an applied magnetic field. Finally, we showcase some of the applications that are currently investigated at ONERA and provide directions for future work.

2. Magnetohydrodynamics modelling

2.1 MHD model

The physics of atmospheric re-entry encompasses very different physics regimes with an accordingly broad variety of models. From the large Knudsen numbers regimes at high altitudes ($\gtrsim 60$ km) to the local thermodynamic equilibrium (LTE) continuum regime at low altitudes, simulation of a full re-entry scenario remains a very challenging objective. As a result, most of numerical studies nowadays still consider the modelling of a steady-state configuration at a given condition of pressure (altitude) and velocity. This method holds as long as characteristic relaxation times of the physical processes at work are smaller than characteristic time of the re-entry trajectory. Here we consider the continuum description of the encountered flow using the classical multi-species Navier-Stokes set of equations describing the dynamics of a viscous fluid:

DOI: 10.13009/EUCASS2023-929

$$\frac{\partial \rho_s}{\partial t} + \nabla \cdot (\rho_s \mathbf{v}) - \nabla \cdot (\rho D_s \nabla y_s) = 0 \tag{1}$$

$$\frac{\partial}{\partial t}(\rho \mathbf{v}) + \nabla \cdot (p\widetilde{\mathbf{I}} + \rho \mathbf{v} \times \mathbf{v} - \widetilde{\tau}) = \mathbf{j} \times \mathbf{B} \tag{2}$$

$$\frac{\partial}{\partial t}\left[\rho\left(\epsilon + \frac{v^2}{2}\right)\right] + \nabla\left[\rho \mathbf{v}\left(h + \frac{v^2}{2}\right)\right] - \widetilde{\tau} \cdot \mathbf{v} - \lambda \nabla T - \nabla \cdot \left(\rho \sum_s h_s D_s \nabla y_s\right) = \mathbf{j} \cdot \mathbf{E} \tag{3}$$

Here ρ_s/ρ is the species/fluid mass density, $\mathbf{v}$ the fluid velocity, D_s the mass diffusivity of species s, y_s the mass fraction of species s, $\widetilde{\tau}$ the stress tensor, p the thermal pressure, $\mathbf{j}$ the electrical current, $\mathbf{B}$ the magnetic field, ϵ the fluid internal energy, h the fluid enthalpy, λ the thermal conductivity and $\mathbf{E}$ the electric field.

As can be seen from Eq. 2 and 3, two source terms in the RHS are present with clear dependency on the electrical current $\mathbf{j}$. The term $\mathbf{j} \times \mathbf{B}$ corresponds to the Lorentz force whereas $\mathbf{j} \cdot \mathbf{E}$ corresponds to electric field work. These quantities need to be solved alongside the classical "fluid" quantities. This can be done using electrostatic theory considering the electric field derives from an electric potential, $\mathbf{E} = -\nabla V$, and solving the charge conservation equation:

$$\nabla \cdot \mathbf{j} = 0 \tag{4}$$

which is combined with the resistive MHD Ohm's law,

$$\mathbf{j} = \sigma(\mathbf{E} + \mathbf{v} \times \mathbf{B}) \tag{5}$$

with σ being the electrical conductivity. A Poisson-type elliptic equation on the electric potential V can then be obtained, describing the fact that no volumetric net charge creation is possible. In Ohm's law 5, the $\mathbf{v} \times \mathbf{B}$ terms describes the fact that in the conductor (here the flow) frame, the electric field is $\mathbf{E}' = \mathbf{E} + \mathbf{v} \times \mathbf{B}$ therefore in this frame we recognise the well known form of the Ohm's law $\mathbf{j} = \sigma \mathbf{E}'$. The above system of equations forms the low-magnetic Reynolds number (R_m) version of the magnetohydrodynamics equations. In the context of re-entry MHD, the dimensionless number R_m can be found to correspond to the ratio of the induced-to-applied magnetic field. In the case of a small R_m ($\lessapprox 0.1$), a situation typically assumed here, the magnetic field $\mathbf{B}$ is stationary even if allowed to be inhomogeneous. This simplifies greatly the problem with only the electric potential V to be solved. The knowledge of V allows estimation of the currents according to 5 and therefore computation of the sources terms present in Eq. 2 and 3.

2.2 Numerical strategy to model MHD re-entry

The set of equations presented in the previous section is solved by a two-code approach where the Navier-Stokes equations with MHD source terms are treated using the ONERAs CEDRE[5] platform whereas the charge conservation equation 4 is solved using the TARANIS code also developed at ONERA.[6] CEDRE is ONERA's multi-physics simulation HPC platform. It includes numerous physics solvers among which the finite-volume CHARME fluid solver is of particular interest for our work. It supports unstructured meshes, Euler/Navier-Stokes multi-species solvers with tabulated real gas properties capabilities. LTE or non-equilibrium chemistry reactions are supported, typically with Arrhenius-type rates. Standard scheme for spatial discretization is of MUSCL-type with explicit and implicit (e.g. GMRES) methods available for time integration of the PDEs. Additional solvers include: radiative transport (ASTRE), eulerian (SPIREE) or lagrangian (SPARTE) dispersed phase, thermal transfer in solids (ACACIA)... TARANIS is a finite-volume MHD code supporting unstructured meshes, electrostatic, magnetoquasistatic (among others) solvers with integration of widespread linear system solving library (PETSc). It includes extended MHD capabilities (Hall effet, ion slip) as well as an internal compressible fluid solver with tabulated real gas properties and a radiation transport module.

Transfers between the two codes are done using the CWIPI library.[5] The general strategy is pictured schematically in Fig.1. At every time step, CEDRE sends to TARANIS the pressure, temperature, mass fractions and velocity distributions whereas TARANIS sends the momemtum and energy source terms described in the previous section. Thermodynamical quantities received by TARANIS are used to compute the electrical conductivity whereas the velocity field is needed for computation of the $\mathbf{v} \times \mathbf{B}$ component of the Omh's law 5. In the case of an LTE gas, conductivity is deduced form tabulated values obtained using the Sethi code described in the next section. When modelling chemically non-equilibrium flows, mass fractions received by TARANIS are used alongside tabulated collisional cross sections from the LXCAT database[7] in order to compute the conductivity.

DOI: 10.13009/EUCASS2023-929

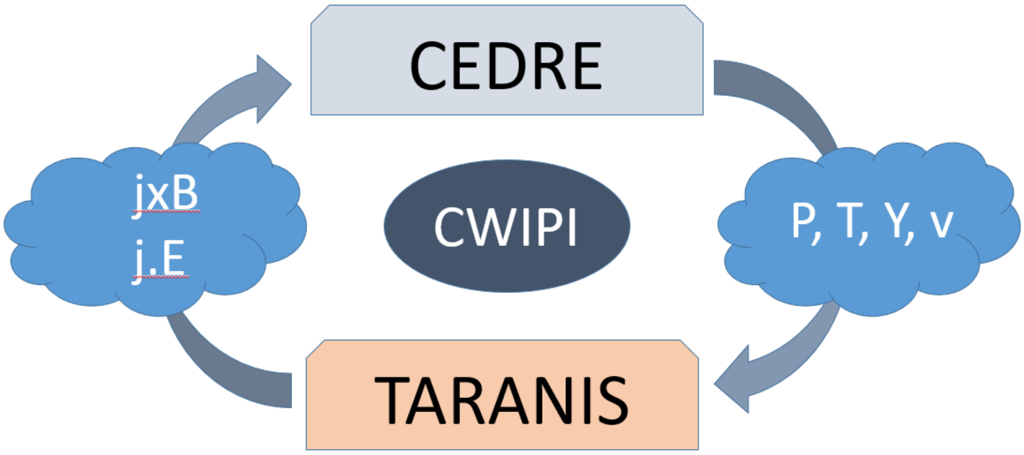

Figure 1: Schematic of coupling between main numerical tools used for modelling MHD re-entry: CEDRE and TARANIS

2.3 Re-entry relevant gas properties for arbitrary mixtures: Sethi

From the previous discussion, it is clear that a central point to the numerical modelling of the atmospheric re-entry of an magnetically-assisted vehicle lies on the thermodynamical and transport properties of the encountered gas that is possibly contaminated with heat shield ablation products, whether desired or not. To address this problem, we have developed a numerical, user-friendly, python tool named Sethi. This code is able to generate tabulated thermodynamics and transport data for both the CEDRE and the TARANIS codes. It computes thermodynamical quantities from partition functions with tabulated atomic energy levels taken for example from the NIST databse.[8] For molecular species energy levels, we follow Drellishak[9] method to take into account coupling between electronic, rotational and vibrational energy modes. Spectroscopic tables from the literature are used to reconstruct molecular levels.[10] Collective effects are somewhat introduced in the model as partition functions are truncated using the minimum value between the Fermi and Griem cutoff.[11] When a mixture is defined, molar fractions at a given pressure and temperature are found by using the Gibbs free energy minimization method.[12] Transport coefficients are computed according to the Chapman-Enskog theory[13] where quantities depend on the binary collision integrals and corresponding interaction potentials. Analytical expressions for collision integrals with Debye-screened coulomb potential are used for charged-charged interactions (see[14]). Neutral-neutral and neutral-charged collision integrals are evaluated using tabulated fits from the literature if available (see for example[15]) or computed directly by defining a binary interaction potential (in a similar way to[16]).

An extended amount of work has been performed on comparing results form the Sethi code to available data in the literature. As an example, we provide in Fig.2 comparisons of thermodynamical (densities, enthalpy and heat capacicty at constant pressure) and transport (electrical conductivity) quantities of an argon mixture with the result of Ref.[17] In general, results show very good agreement with some differences observed in conductivity values. This could be due to different choices in the collision integrals and interaction potentials.

Alkali seeding of the re-entry flow has been suggested in order to dramatically increase the MHD effects around re-entering vehicles.[18] As a rather simple way of modelling seeding in LTE regimes (low altitudes), we have introduced in Sethi the possibility to generate multi-dimensional thermodynamic and transport tables for both TARANIS and CEDRE. Typically, a dataset of cesium-seeded air would be generated using (P,T,Y_{C_s}) tabulated data, the cesium mass fraction Y_{C_s} ranging from 0 to unity and a zero fraction corresponding to pure air. Because seeding is generally not done in a homogeneous way (for example produced by an alkali-doped ablative heat shield), mass diffusion in the LTE regime needs some special treatment. We adopt here the quasi-binary approximation approach in order to compute diffusion coefficients within a two-species model (only two equations of mass conservation 1). With this approach and for earth re-entry for example, the eight air species (O_2, N_2, NO, O, N, NO^+, O^+, N^+) and the two cesium species Cs and Cs^+ are combined into two "gases" A and B. The problem is then treated as the diffusion of gas B into gas A using the following definition:[19]

$$D_{AB} = \frac{\left[\sum_{i=2}^{p}(1+Z_i)x_i\right]\left[\sum_{i=p+1}^{q}(1+Z_i)x_i\right]}{\sum_{i=2}^{p} x_i \sum_{j=p+1}^{q} x_j/D_{ij}} \tag{6}$$

where Z_i is the charge state of species i, x_i are the molar fractions and D_{ij} are the binary diffusion coefficients calculated from.[20] Air gas A corresponds to species from 2 to p and cesium gas B to species from p+1 to q.

DOI: 10.13009/EUCASS2023-929

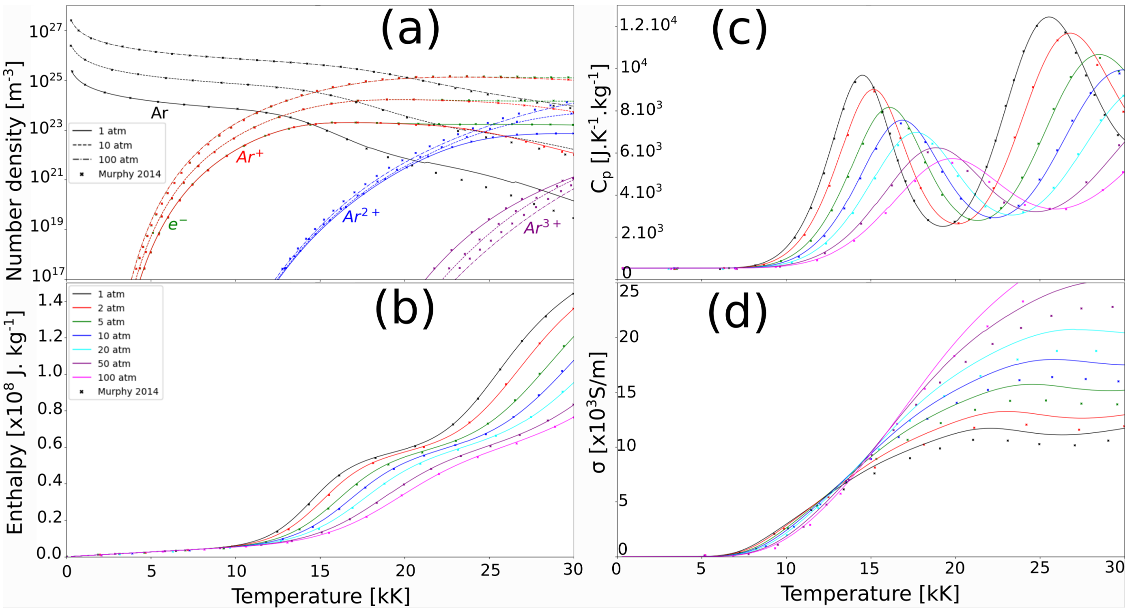

Figure 2: (a) Number densities, (b) enthalpy, (c) heat capacity at constant pressure and (d) electrical conductivity of an argon LTE mixture (Ar, Ar^+, Ar^{2+}, Ar^{3+} and electrons) obtained with the Sethi code (full lines). For comparisons, dots are from Ref.[17]

As an example of a typical plasma LTE composition for a mixture of air and alkali metal, in this case cesium, we show in Fig.3(a) molar fractions temperature dependency (from 300 to 15 kK) for a 10 % seeded air at atmospheric pressure. One can see the expected start of dissociation of O_2 and N_2 molecules for temperatures above $\sim$ 2000 K. Substantial ionization of atomic nitrogen and oxygen starts above $\sim$ 8000-9000 K whereas, due to its very low ionization potential ($\sim$ 3.9 eV), cesium starts being ionized at only $\sim$ 2000 K. A direct consequence of the presence of cesium can be observed in Fig.3(b) where electrical conductivity is shown for different cases: pure air, 1, 5 and 20 % Cs-seeded air. We see that when cesium is present, substantial conductivity values are obtained at low temperatures. At high temperatures, conductivity becomes basically independent of cesium fraction.

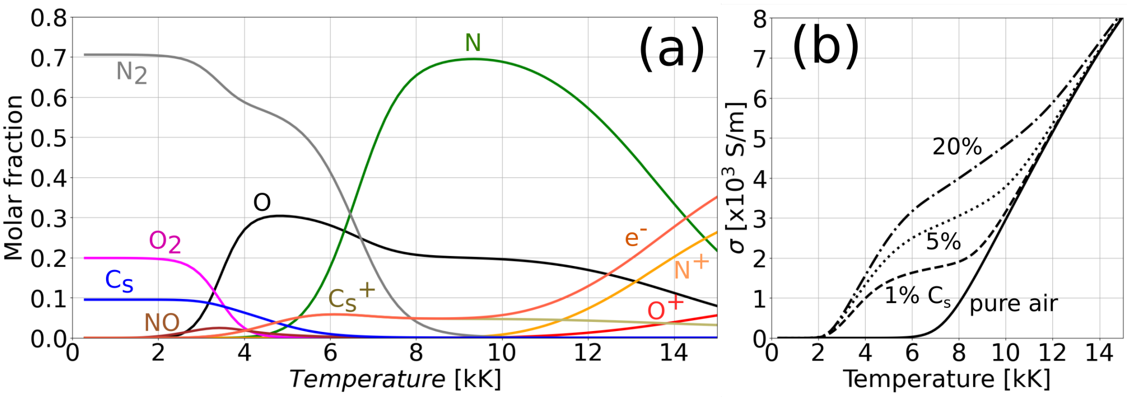

Figure 3: Results from Sethi: (a) Temperature dependency of molar fractions of an LTE air-cesium mixture at atmospheric pressure(10 % of cesium) (b) Electrical conductivity of different air-cesium mixtures

2.4 Modelling of non-equilibrium flows: a three-temperatures model

The question of identifying the correct regime of the re-entry flow is a complex task. One way of looking at this problem is evaluating the binary scaling parameter ρR_n $[kg.m^{-2}]$ (R_n is typically the re-entry vehicle nose radius).[21] As the value of this parameter increases (higher densities/lower altitudes or larger vehicles), we transition from highly non-equilibrium flow (thermal and chemical non-equilibrium) to LTE flows with intermediate regime being thermal

DOI: 10.13009/EUCASS2023-929

equilibrium but thermal non-equilibrium. For vehicle velocities greater than ~ 5 km/s, transitions occur very roughly at $\rho R_n \approx 10^{-4}\ kg.m^{-2}$ for full non-equilibrium to intermediate regime and $\rho R_n \approx 10^{-2}\ kg.m^{-2}$ for intermediate to LTE. In order to model a full trajectory or at least a multi-sampling of a trajectory (with steady state for each chosen point of the trajectory), one need to take into account multi-modes energy distribution over finite timescales. To achieve this, we have implemented a three-temperatures model into the TARANIS code. We therefore keep track, in addition of the total energy, of the vibrational energy energy per unit volume $\rho\mathcal{E}_v$ and the translational electronic energy per unit volume $\rho\mathcal{E}_e$:[22]

$$\frac{\partial}{\partial t}(\rho\mathcal{E}_v) + \boldsymbol{\nabla}\cdot(\rho\mathcal{E}_v\boldsymbol{v}) - \boldsymbol{\nabla}\cdot(\lambda_v\boldsymbol{\nabla}T_v) - \boldsymbol{\nabla}\cdot\left(\rho\sum_{s=m}\mathcal{E}_{vs}D_s\boldsymbol{\nabla}y_s\right) = \dot{\Omega}_v \tag{7}$$

with

$$\dot{\Omega}_v = \dot{\Omega}^{VT} + \dot{\Omega}^{VE} - \dot{\Omega}_v^{D}.$$

where the $\dot{\Omega}^{VT}$ term represents the energy exchange between vibrational and translational modes due to collisions, the $\dot{\Omega}^{VE}$ term the energy exchange between vibrational and electronic modes and finally the $\dot{\Omega}_v^{D}$ term which represents the vibrational energy lost or gained due to molecular dissociation or recombination.

and:

$$\frac{\partial}{\partial t}(\rho\mathcal{E}_e) + \boldsymbol{\nabla}\cdot(\rho\mathcal{E}_e\boldsymbol{v}) + p_e\boldsymbol{\nabla}\cdot\boldsymbol{v} - \boldsymbol{\nabla}\cdot(\lambda_e\boldsymbol{\nabla}T_e) - \boldsymbol{\nabla}\cdot(\rho h_e D_e\boldsymbol{\nabla}y_e) = \frac{j^2}{\sigma} + \dot{\Omega}_e \tag{8}$$

with

$$\dot{\Omega}_e = \dot{\Omega}^{ET} - \dot{\Omega}^{VE} - \dot{\Omega}_e^{D} - \dot{\Omega}_e^{I} + \dot{\Omega}_e^{C}.$$

where the $\dot{\Omega}^{ET}$ term represents the energy exchange between between electrons and heavy particles due to elastic collisions, the $\dot{\Omega}_e^{D}$ term the energy loss due to electron impact dissociation, the $\dot{\Omega}_e^{I}$ term the energy loss due to electron impact ionization and finally the $\dot{\Omega}_e^{C}$ term the energy gain due to electron production. Note here the ohmic heating j^2/σ term present as a source term for electron energy.

As total internal energy is the sum of the translational and rotational energy of heavy species, the vibrational energy of molecules and the translational energy of electrons, the translational and rotational energy per unit volume $\rho\mathcal{E}_{tr}$ can be retrieved easily as $\rho\mathcal{E}_{tr} = \rho\mathcal{E} - \rho\mathcal{E}_v + \rho\mathcal{E}_e$. Note here that equilibration between rotational and heavy translational modes is assumed.

Alongside this multi-energy model, a multi-temperature chemistry module has also been implemented into TARANIS with the use of the RADAU method adapted for stiff problems.[23] Arrhenius-type reactions rates are defined using one or a combination of the available three temperatures: electronic T_e, vibrational T_v and heavy-rotational T. The choice depends on the reaction type with for example reactions involving electrons being at the electronic temperature. Forward T_f and T_b backward temperatures used for typical reactions are indicated in Tab. 1. When using the chemistry module, Eq.1 is of course modified by addition of the proper mass source termsin the RHS for each of the species included in the model.

Table 1: Controlling temperatures for various reaction mechanisms.

Reaction	T_f	T_b
Ionization by neutral impact	T	T
Ionization by electron impact	T_e	T_e
Dissociation by neutral impact	$\sqrt{TT_v}$	T
Dissociation by electron impact	T_e	T_e
Neutral exchange	T	T
Charge exchange	T	T
Associative ionization	T	T_e
Reassociation	T	T

3. Some examples of applications

3.1 Modelling of laboratory hypersonics experiments in expansion tubes

A sustained effort to confront and validate theoretical models and numerical tools with experiments is of crucial importance. Experiments aiming at generating and quantifying an MHD effect on a hypersonic flow are typically performed

DOI: 10.13009/EUCASS2023-929

in high-enthalpy wind tunnels[24] (necessary to obtain enough ionization of the flow) or in shock tubes facilities.[3] Fine knowledge of the freestream flow properties is usually a delicate question and substantial work is typically needed in order to characterize correctly all relevant parameters. In particular, ionization level of the flow is an important question when dealing with MHD experiments. The group at university of Queensland has in this context produced detailed description of their shock-tube test conditions and have shown in particular that they are able to produce basically non-ionized freestream flows. Interestingly, they have performed experiments in argon gas, allowing for easier comparisons with simulations due to simpler thermodynamics and chemical properties. An ongoing work is carried out at ONERA to numerically reproduce their setup. It consists of an either insulated or conductive magnetized sphere of diameter ~ 38 mm (see inset in Fig.4(a)). Looking at specific test conditions, the incoming flow is characterized by T=1112 K, P=427 Pa and v=6306 m/s. Some preliminary results are shown in Fig.4 for magnetic field at sphere surface of ~ 1 T. In Fig.4(a) the electromotive $\mathbf{v} \times \mathbf{B}$ field is visualized with clear observation of the shock discontinuity acting on the velocity. Azimuthal induced electrical currents are obtained by multiplication with the conductivity σ: $\mathbf{j} = \sigma \mathbf{v} \times \mathbf{B}$. To visualize influence of non equilibrium effects, we show in Fig.4(b), (c) and (d) comparisons of temperature, conductivity and Lorentz forces maps obtained for LTE or in chemical nonequilibrium (noted "NE" in the figure). In this regime and because of the small size of the sphere, large differences are observed. Chemical reactions included for non-equilibrium calculations are given below:

$$\mathrm{Ar} + \mathrm{Ar} \underset{k_{-1}}{\overset{k_1}{\rightleftarrows}} \mathrm{Ar}^+ + \mathrm{e}^- + \mathrm{Ar}$$

$$\mathrm{Ar} + \mathrm{Ar}^+ \underset{k_{-2}}{\overset{k_2}{\rightleftarrows}} \mathrm{Ar}^+ + \mathrm{e}^- + \mathrm{Ar}^+$$

$$\mathrm{Ar} + \mathrm{e}^- \underset{k_{-3}}{\overset{k_3}{\rightleftarrows}} \mathrm{Ar}^+ + \mathrm{e}^- + \mathrm{e}^-$$

with forward and backward arrows indicating direct and reverse reactions. The reaction rates k_i are estimated using Arrhenius-type expression $AT^B e^{T/T_a}$ with values of A, B and T_a coefficients deduced from Queensland work:

- $k_1 : A = 0.1045\ m^3.mol^{-1}.s^{-1},\ B = 1.418,\ T_a = 101500\ K$
- $k_2 : A = 0.1045\ m^3.mol^{-1}.s^{-1},\ B = 1.418,\ T_a = 101500\ K$
- $k_3 : A = 976.8\ m^3.mol^{-1}.s^{-1},\ B = 1.418,\ T_a = 101500\ K$

Reverse rates are deduced from the forward rates using the equilibrium constant.

Kinetic energy of the incoming flow is in one case (LTE) converted instantaneously in thermal and chemical reactions whereas when finite-rate chemical reactions are allowed most of the energy is converted solely into kinetic (translational) energy. This explains the large differences in temperatures observed in Fig.4(b). Because ionizing reactions do not have time to proceed, ionization degree and resulting electrical conductivity is much smaller in the non-equilibrium case (see Fig.4(c)). As a consequence, Lorentz forces are also of lower magnitudes in the non-equilibrium case, Fig.4(d). Despite the higher values of magnetic forces in the LTE case, the shock-to-nose distance is smaller in this case (see Fig.4(b)). This is because the hotter post-shock plasma in the non-equilibrium case is of lower mass density and therefore steady-state implies a thicker layer of the shocked flow. Work is underway to include multi-temperature effects to these simulations.

3.2 Modelling of martian re-entry

Here we present numerical results from the highly non-equilibrium conditions of martian re-entry. Because of atmospheric pressure ~ 100 times lower than in earth atmosphere, most if not all of the re-entry trajectory can actually be considered as being in a non-equilibrium regime. We make use of the previously described three-temperatures model to investigate the mars re-entry of a pathfinder-type geometry.[26] A magnetic dipole is placed near the nose of the vehicle as it can be seen in Fig.5(a) where colormap corresponds to B-field magnitude (0.3 T at maximum on vehicle surface) and black lines correspond to the streamlines of the dipolar magnetic field. Some results from our 2D axisymmetric simulations are shown in Fig.5(b) with on top the molar fraction of electrons and bottom the electrical conductivity. Freestream conditions here correspond to a velocity of 6.5 km/s and a martian altitude of 50 km. Maximum fraction of electron is ~ 4.10^4 close to the nose, a relatively small value mostly due to chemical non-equilibrium. Maximum value of conductivity is ~ 120 S/m also in the post-shoc region close to the nose. In the 2D map of Fig.5(c) we show colormap of the electron temperature. A first lineout is taken along the stagnation line (top curves) where clear evidence of energy decoupling is observed in a small region close to the shock itself. Because most of the initial kinetic energy is carried

DOI: 10.13009/EUCASS2023-929

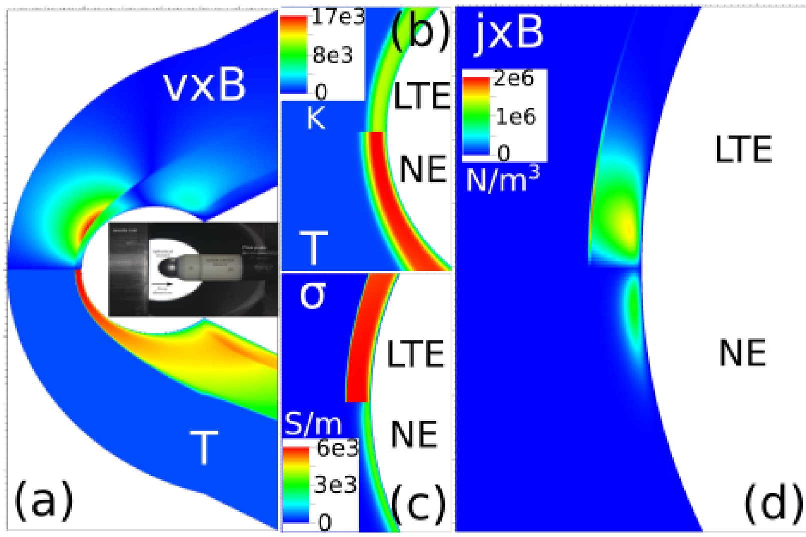

Figure 4: Numerical results on the Queensland's laboratory setup shown as inset in (a) (taken from[25]). (a) Electromotive field $\mathbf{v} \times \mathbf{B}$ and temperature and zoom on (b) temperature (c) electrical conductivity (d) and Lorentz force magnitude are displayed for both the LTE and the chemically non-equilibrium regimes ("NE"). Flow is always from left to right.

out by the heavy particles, it is the associated temperature T (red curve) that is maximum at the shock with a peak at $\sim$ 16 000 K. Electronic and vibrational temperatures are $\sim$ 7000-8000 K, roughly two times smaller. Now looking at temperatures downstream, we observe a relatively spread region where substantially hotter electrons are present. A lineout across this region (bottom right image) show that there electron temperature is $\sim$ 12 000 K whereas vibrational and heavy temperature is roughly two times lower at $\sim$ 6000-7000 K. We attribute this effect to the localized strong ohmic heating of the electron population (it is in this region that the flow has maximum $\mathbf{v} \times \mathbf{B}$ value). These result could be of importance for MHD effects since in particular the electrical conductivity depends solely on the electron temperature. These preliminary results which are yet to be studied in detail tend to show strong non-homogeneous and non-equilibrium effects associated to the presence of the magnetic field. Further investigation is needed to clarify the complete picture about these mechanisms, in particular their dependency to freestream conditions.

3.3 Hall effect in re-entry flows

As a last example, we quickly present the effect of an extended MHD mechanism, namely the Hall effect. It can be included in our model by modification of the definition of the Ohm's law. Indeed if we now write:

$$\boldsymbol{j} = \widetilde{\boldsymbol{\sigma}} \cdot (\boldsymbol{E} + \boldsymbol{v} \times \boldsymbol{B}) \tag{9}$$

with

$$\widetilde{\boldsymbol{\sigma}} = \begin{pmatrix} \sigma_P & -\sigma_H & 0 \\ \sigma_H & \sigma_P & 0 \\ 0 & 0 & \sigma_e \end{pmatrix}.$$

and,

$$\sigma_e = \frac{n_e q_e^2}{m_e \nu_e}.$$

$$\sigma_H = \frac{\beta_e}{1+\beta_e^2}\sigma_e$$

$$\sigma_P = \frac{1}{1+\beta_e^2}\sigma_e.$$

we now have have a tensorial expression of the electrical conductivity. σ_e is the "standard" conductivity used in the resistive Ohm's law 5. σ_H and σ_P are respectively called the Hall and the Pedersen conductivities. β_e is the electron Hall parameter defined as

$$\beta_e = \frac{\omega_c}{\nu_e}$$

DOI: 10.13009/EUCASS2023-929

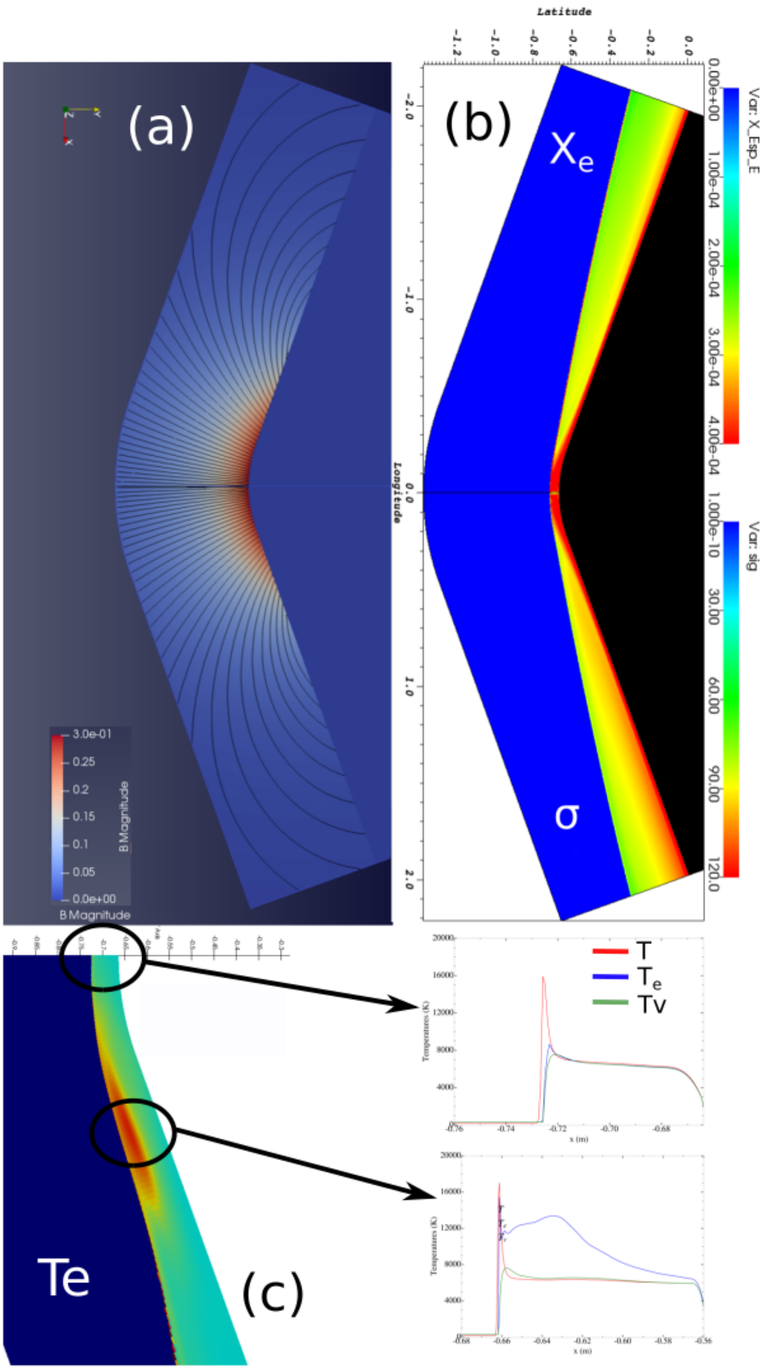

Figure 5: Simulation of mars pathfinder-type re-entry vehicle in martian atmospheric conditions (50 km, 6.5 km/s). (a) Colormap of magnetic field magnitude and streamlines of magnetic field (b) top half: electron molar fraction bottom half: electrical conductivity (c) left: colormap of electronic temperature and right: lineouts at different positions of the electornic temperature. FLow is always from left to right.

with the electron cyclotron frequency $\omega_c = |q_e| B/m_e$ and ν_e the total electron collision frequency. For sake of simplicity, when deriving expression for the generalized Ohm's law 9, it was assumed that B-field was along z-direction. From this new expression, we can see that the current will in general not be aligned with the effective electric field $\boldsymbol{E} + \boldsymbol{v} \times \boldsymbol{B}$. It will however be a very good approximation when β_e approaches zero, that is for non-magnetized electrons. This effect has been implemented in TARANIS and a visual demonstration of one of its consequences on MHD re-entry is shown in Fig.6. Here we show on the left the distribution of Hall parameter for an magnetized (1 T on vehicle surface) axisymmetric hemispheric re-entry geometry in earth atmosphere at 6.5 km/s and an altitude of 60 km. For this high altitude/low density regime, collisions are weak enough to make Hall parameters much larger than one, making

DOI: 10.13009/EUCASS2023-929

tensorial conductivity expressed in Eq.9 relevant. Without Hall effect it is expected to observe from this configuration only out-of-plane electrical currents because magnetic moment is oriented in the plane, along the top symmetry axis. Now if we look at the right image in Fig.6, in-plane "Hall" currents are clearly circulating around the vehicle in the conductive post-shock plasma. We note here that the vehicle body is considered in our simulation as an insulator and therefore current forms closed loop in the plasma. A well known consequence of the circulation of these Hall currents is a potentially strong deterioration of the primary desired MHD effect involving flow deceleration through azimuthal electrical currents induced in the $\mathbf{v} \times \mathbf{B}$ direction.[27]

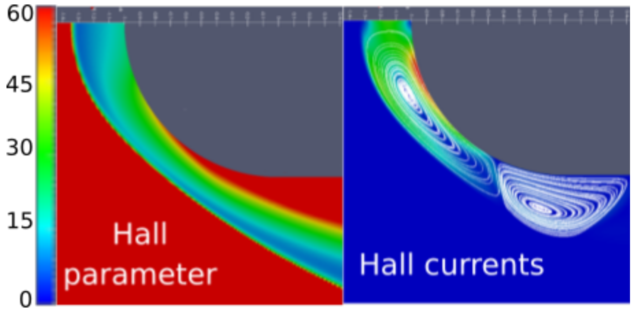

Figure 6: Hall effect on a simple 2D axisymmetric hemispherical geometry in earth atmosphere. The flow is from the left to the right with freestream condition corresponding to v=6.5 km/s and 60 km altitude. On left image is represented the Hall parameter whereas on the right image current streamlines of the in-plane "Hall" currents are shown.

4. Conclusion

MHD techniques could bring novel solutions to the problems of heating and trajectory control for space vehicles re-entry. We develop at ONERA an extended suit of numerical tools with the aim of capturing the physical mechanisms at work when a magnetic field is applied to the post-shock ionized flow.

The problem is treated by coupling the ONERA's CEDRE platform to our in-house MHD code TARANIS. We are able to model complex geometries with multi-materials both for the fluid and the electromagnetism. Electric potential is solved alongside fluid quantities. For an interaction parameter high enough, strong modification of the flow is possible. It is then possible to consider efficient MHD mitigation of heat transfert from the flow to the vehicle as well as the modification of the aerodynamic coefficients. Future works include the improvement of our numerical tools with the capability to model self-consistently the seeded heat shield ablation, turbulent effects... We also aim to validate our codes and models with MHD experiments on ONERA and/or academic wind tunnels or shock tubes.

References

[1] EL Resler Jr and WR Sears. The prospects for magneto-aerodynamics-correction and addition. *Journal of the Aerospace Sciences*, 26(5):318–318, 1959.

[2] Richard W Ziemer and William B Bush. Magnetic field effects on bow shock stand-off distance. *Physical Review Letters*, 1(2):58, 1958.

[3] Daniel R Smith, David E Gildfind, David J Mee, Christopher M James, and Barry V Allsop. Magnetohydrodynamic drag force measurements in an expansion tunnel using a stress wave force balance. *Experiments in Fluids*, 61:1–15, 2020.

[4] Andrea Lani, Vatsalya Sharma, Vincent F Giangaspero, Stefaan Poedts, Alan Viladegut, Olivier Chazot, Jasmine Giacomelli, Johannes Oswald, Alexander Behnke, Adam S Pagan, et al. A magnetohydrodynamic enhanced entry system for space transportation: Meesst. *Journal of Space Safety Engineering*, 10(1):27–34, 2023.

[5] A Refloch, B Courbet, A Murrone, P Villedieu, C Laurent, P Gilbank, J Troyes, L Tessé, G Chaineray, JB Dargaud, et al. Cedre software. *Aerospace Lab*, (2):p–1, 2011.

[6] Aymeric Bourlet, Julien Labaune, Fabien Tholin, Axel Vincent, François Pechereau, and Christophe O Laux. Numerical model of restrikes in dc gliding arc discharges. In *AIAA SCITECH 2022 Forum*, page 0831, 2022.

DOI: 10.13009/EUCASS2023-929

[7] Emile Carbone, Wouter Graef, Gerjan Hagelaar, Daan Boer, Matthew M Hopkins, Jacob C Stephens, Benjamin T Yee, Sergey Pancheshnyi, Jan Van Dijk, and Leanne Pitchford. Data needs for modeling low-temperature non-equilibrium plasmas: the lxcat project, history, perspectives and a tutorial. *Atoms*, 9(1):16, 2021.

[8] Yuri Ralchenko and Alexander Kramida. Development of nist atomic databases and online tools. *Atoms*, 8(3):56, 2020.

[9] KS Drellishak, DP Aeschliman, and Ali Bulent Cambel. Partition functions and thermodynamic properties of nitrogen and oxygen plasmas. *The Physics of Fluids*, 8(9):1590–1600, 1965.

[10] D Pagano, A Casavola, LD Pietanza, M Capitelli, G Colonna, D Giordano, and L Marraffa. Internal partition functions and thermodynamic properties of high-temperature jupiter-atmosphere species from 50k to 50,000 k. *ESA Scientific Technical Review, vol. 257*, 257, 2009.

[11] Gianpiero Colonna and Annarita Laricchiuta. Thermodynamic and transport properties of equilibrium debye plasmas. *Entropy*, 22(2):237, 2020.

[12] Sanford Gordon and Bonnie J McBride. Computer program for calculation of complex chemical equilibrium compositions and applications. part 1: Analysis. Technical report, 1994.

[13] D. B. Spalding. The molecular theory of gases and liquids.j. o. hirschfelder, c. f. curtiss and r. b. bird. john wiley,new york. chapman amp; hall, london, 1954. 1,219 pp.diagrams. 160s. *The Aeronautical Journal*, 59(531):228â228, 1955.

[14] Hong-sup Hahn, EA Mason, and Francis J Smith. Quantum transport cross sections for ionized gases. *The Physics of Fluids*, 14(2):278–287, 1971.

[15] Annarita Laricchiuta, Domenico Bruno, Claudio Catalfamo, Francesco Pirani, G Colonna, P Diomede, Damiano Pagano, C Gorse, S Longo, R Celiberto, et al. Transport properties of high-temperature mars-atmosphere components. In *39th AIAA Thermophysics Conference*, page 4043, 2007.

[16] Gianpiero Colonna and Annarita Laricchiuta. General numerical algorithm for classical collision integral calculation. *Computer Physics Communications*, 178(11):809–816, 2008.

[17] Anthony B Murphy and Eugene Tam. Thermodynamic properties and transport coefficients of arc lamp plasmas: argon, krypton and xenon. *Journal of Physics D: Applied Physics*, 47(29):295202, 2014.

[18] Sergey Macheret, Mikhail Shneider, and Graham Candler. Modeling of mhd power generation on board reentry vehicles. In *42nd AIAA Aerospace Sciences Meeting and Exhibit*, page 1024, 2004.

[19] JA Bakken. Modelling of fluid flow, heat transfer and diffusion in arcs. *Journal of high temperature chemical processes*, 3(6):677–688, 1994.

[20] JT Vanderslice, Stanley Weissman, EA Mason, and RJ Fallon. High-temperature transport properties of dissociating hydrogen. *The Physics of Fluids*, 5(2):155–164, 1962.

[21] Klaus Hannemann, Jan Martinez Schramm, Alexander Wagner, and Giannino Ponchio Camillo. The high enthalpy shock tunnel göttingen of the german aerospace center (dlr). *Journal of large-scale research facilities JLSRF*, 4(A133):1–14, 2018.

[22] Peter A Gnoffo. *Conservation equations and physical models for hypersonic air flows in thermal and chemical nonequilibrium*, volume 2867. National Aeronautics and Space Administration, Office of Management â¦, 1989.

[23] Gerhard Wanner and Ernst Hairer. *Solving ordinary differential equations II*, volume 375. Springer Berlin Heidelberg New York, 1996.

[24] Viviana Lago, Hugo Noubel, Mélodie Creange, Jonathan Jaegly, and Juliette Prezeau. Modification of the bow shock shape and thermal effects with mhd actuator in supersonic low pressure plasma flows. In *HiSST: 2nd International Conference on High-Speed Vehicle Science Technology*, 2022.

[25] David Gildfind, Daniel Smith, Owen Thompson, Peter Jacobs, Richard Morgan, Rory Kelly, and Tim McIntyre. Evaluation of electrically insulating coatings for magnetohydrodynamic aerobraking experimentation. 2019.

DOI: 10.13009/EUCASS2023-929

[26] Minkwan Kim and Iain D Boyd. Effectiveness of a magnetohydrodynamics system for mars entry. *Journal of Spacecraft and Rockets*, 49(6):1141–1149, 2012.

[27] Hirotaka Otsu, Detlev Konigorski, and Takashi Abe. Influence of hall effect on electrodynamic heat shield system for reentry vehicles. *AIAA journal*, 48(10):2177–2186, 2010.